

Micromagnetic Simulations Study of Skyrmions in Magnetic FePt Nanoelements

Leonidas N. Gergidis* ¹, Vasileios D. Stavrou¹, Drosos Kourounis², and Ioannis Panagiotopoulos¹

¹Department of Materials Science and Engineering, University of Ioannina, 45110 Ioannina, Greece

²NEPLAN AG, CH-8700 Küsnacht (ZH), Switzerland

November 26, 2021

Abstract

The magnetization reversal in 330nm triangular prismatic magnetic nanoelements with variable magnetocrystalline anisotropy similar to that of partially chemically ordered FePt is studied using micromagnetic simulations employing Finite Element discretizations. Several magnetic properties including the evaluation of the magnetic skyrmion number S are computed in order to characterize magnetic configurations exhibiting vortex-like formations. Magnetic vortices and skyrmions are revealed in different systems generated by the variation of the magnitude and relative orientation of the magnetocrystalline anisotropy direction, with respect to the normal to the triangular prism base. Micromagnetic configurations with skyrmion number greater than one have been detected for the case where magnetocrystalline anisotropy was normal to nanoelement's base. For particular magnetocrystalline anisotropy values three distinct skyrmions are formed and persist for a range of external fields. The simulation-based calculations of the skyrmion number S revealed that skyrmions can be created for magnetic nanoparticle systems lacking of chiral interactions such as Dzyaloshinsky-Moriya, but by only varying the magnetocrystalline anisotropy.

1 Introduction

Magnetic nanoparticles and nanostructures find numerous applications in a wide variety of scientific fields including information signal processes, spin devices, high density storage media, magnetic sensors, medicine and biology [41, 20, 35, 2, 14]. Nowadays progress in nanoscale material growth have allowed the synthesis and fabrication of nanoparticles in a wide range of shapes and sizes [37, 44, 16]. Their magnetic response is of paramount importance and could be associated with geometrical and materials factors; thus, a lot of effort has been devoted to experimental, simulation and theoretical studies. In par-

ticular, the process of magnetization reversal in magnetic nanoparticles could be exploited, engineered for technological applications but necessitates the knowledge and control over the formation of rather complex micromagnetic structures, such as multiple domain walls, vortices, skyrmions-antiskyrmions and merons [38, 48, 42, 46, 45, 43, 28, 15].

Magnetic skyrmions are vortex-like magnetization configurations. They have been predicted theoretically by Bogdanov et al. [3],[4] long before their experimental detection and discovery [26, 24]. In recent years magnetic skyrmions have attracted a lot of theoretical [13, 22, 23, 39, 5, 21], simulation [9, 18, 40, 32], and experimental [13, 34, 17, 11, 27] attention due to their thermodynamic and topological stability, their small size, and their inherent property of easy movement and repositioning under the application of low or even tiny in-plane electric currents. They seem promising for use in next generation spintronic devices [33, 50] as information carriers, giving the credentials of ultra dense low-cost power storage and the capability to perform logical operations [12]. The next generation magnetic memory devices would rely on the efficient creation and control of magnetic textures, such as magnetic skyrmions using rather tiny electric currents [35, 29, 7, 19]. The aforementioned topological stability is related to the confined skyrmion magnetic configuration, which is predicted to be stable because the individual atomic spins, oriented opposite to those of the surrounding thin-film cannot perform flipping motion. Spins hindered to align themselves with the rest of atoms in confined geometry without overcoming an energy barrier. The origin of the energy barrier is attributed to the "topological protection". The thermodynamic stability of skyrmions is considerably strong and can be attributed to the particular magnetic configuration which can be characterized by a total topological charge described by skyrmion number S [22, 23]. This skyrmion number S is an integer and to this point is being considered having quantized values that cannot be changed continuously. The skyrmion

*lgergidi@uoii.gr; lgergidis@gmail.com

number S is defined as

$$S = \frac{1}{4\pi} \int_A q_{Sk} dA \quad (1)$$

where q_{Sk} is given by the following relation

$$q_{Sk} = \mathbf{m} \cdot \left(\frac{\partial \mathbf{m}}{\partial x} \times \frac{\partial \mathbf{m}}{\partial y} \right). \quad (2)$$

The quantity \mathbf{m} is the unit vector of the local magnetization defined as $\mathbf{m} = \mathbf{M}/M_s$ with \mathbf{M} being the magnetization and M_s the saturation magnetization. The skyrmion number S is a physical and topological quantity that measures how many times \mathbf{m} wraps the unit sphere [47]. The integrated quantity describes the topological density q_{Sk} and has units of nm^{-2} , which are implied throughout the manuscript. In many instances the integrated quantity is also referred as “topological charge”. Surface A is the surface domain of integration and corresponds to the upper or the lower triangular bounding surface of the FePt nanoelement under investigation.

The magnetization reversal in 330 nm triangular prism magnetic nanoelements with variable magnetocrystalline anisotropy (as that of partially chemically ordered FePt) has been studied using Finite Elements micromagnetic simulations in [38]. The simulation results showed that a wealth of reversal mechanisms is possible sensitively depending on the uniaxial magnetocrystalline anisotropy values and directions; the latter may explain the different Magnetic Force Microscopy patterns obtained in such magnetic systems. In addition, the micromagnetic simulations revealed that interesting vortex-like formations can be produced and stabilized in large field ranges and in sizes that can be tuned by the magnetocrystalline anisotropy (MCA) of the material. The aforementioned spontaneous ground states of skyrmion-like configurations were obtained and in other magnetic systems without the implication of chiral interactions such as Dzyaloshinsky-Moriya (DMI) [45, 39, 6, 51, 36, 10, 49].

In the present work a quantitative description is given for the vortex-skyrmionic configurations by calculating the skyrmion number at 0°K obtained for FePt triangular magnetic nanoislands having variable magnetocrystalline anisotropy. The aforementioned calculation can reveal information not readily recognizable by simple visual-inspection of the micromagnetic configurations. Furthermore, the skyrmion number as a function of the applied field along a hysteresis curve can give quantitative information of the reversal mechanisms and energy barriers involved. In what follows we present examples on the numerical calculation of skyrmion number as means of characterizing magnetic configurations and reversal in nanoelements including thin film asymmetric triangular nanoislands.

2 Micromagnetic modeling

2.1 FEM solution of Landau-Lifshitz-Gilbert (LLG) equation

The rate of change of the dynamical magnetization field \mathbf{M} is governed by a nonlinear equation of motion, the Landau-Lifshitz-Gilbert (LLG) equation

$$\frac{d\mathbf{M}}{dt} = \frac{\gamma}{1 + \alpha^2} (\mathbf{M} \times \mathbf{H}_{eff}) - \frac{\alpha\gamma}{(1 + \alpha^2)|\mathbf{M}|} \mathbf{M} \times (\mathbf{M} \times \mathbf{H}_{eff}). \quad (3)$$

In the aforementioned LLG equation $\alpha > 0$ is a phenomenological dimensionless damping constant that depends on the material and γ is the electron gyromagnetic ratio. The effective field that governs the dynamical behavior of the system has contributions from various effects that are of very different nature and can be expressed as $\mathbf{H}_{eff} = \mathbf{H}_{ext} + \mathbf{H}_{exch} + \mathbf{H}_{anis} + \mathbf{H}_{demag}$. Respectively, these field contributions are the external magnetic field \mathbf{H}_{ext} , the exchange field \mathbf{H}_{exch} , the anisotropy field \mathbf{H}_{anis} and the demagnetizing field \mathbf{H}_{demag} .

For the solution of the LLG equation We have performed micromagnetic finite element calculations using the Nmag software [8]. The dimensionless damping constant α was set to 1 in order to achieve fast damping and reach convergence quickly as we are interested in static magnetization configurations. The default convergence criterion for each applied external field step \mathbf{H}_{ext} was that the magnetization should move slower than 1 degree per nanosecond, globally or on average for all spins. The sample was described as a triangular prism with equilateral triangle base of 330 nm and 36 nm in height and is shown in **Fig. 1**. The 36 nm thickness of the film matches that reported in [25] while Okamoto in [31] suggests 24 nm, which is comparable and not expected to lead to qualitatively different behavior. The following frame of reference axes assignment convention was used: x along the triangle height, y along the side perpendicular to x, and z perpendicular to the film plane. The considered finite element mesh for the triangular film under study was generated using the automatic three dimensional (3D) tetrahedral mesh generator Netgen [30]. We have used a 3.4 nm maximum distance between nodes which is lower than the value of the exchange length $l_{ex} = \sqrt{\frac{2A}{\mu_0 M_s^2}} \approx 3.5$ nm. This resulted in 488874 vol-

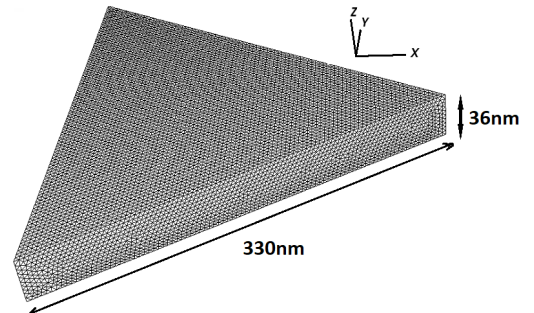


Figure 1: Model geometry and the generated mesh.

ume elements (94800 points) per triangular magnetic island. The material parameters were chosen similar to those typical for bulk FePt with a saturation polarization of $\mu_0 M_s = 1.43T$ ($M_s = 1.138\text{MA/m}$), and an exchange constant $A_{exch} = 11\text{pJ/m}$ which has been found to be independent of the degree of ordering Okamoto [31]. The magnetocrystalline anisotropy (MCA) constant Ku was varied between $Ku = 100\text{kJ/m}^3$ and 500kJ/m^3 , as for Ku exceeding this value the reversal mode was simply homogeneous rotation. The demagnetization factor \mathcal{N} has been estimated to $\mathcal{N} = 0.71$ by the saturation field perpendicular to the triangle for the case of $Ku = 0\text{kJ/m}^3$. We must note that for the range of these MCA values the easy axis remains in-plane as the shape anisotropy contribution $-\frac{1}{2}\mathcal{N}\mu_0 M_s^2 = -580\text{kJ/m}^3$ exceeds Ku for all the cases presented here. Four different directions of the magneto-crystalline anisotropy were tested along x, y, z as well as along the $[111]$ direction. The latter is of interest as in many instances FePt and CoPt films tend to grow with their $\langle 111 \rangle$ crystallographic directions along the film normal resulting an angle of 54.7° to the film normal [1].

The total duration of the micromagnetic simulation was ranging for 1 to 10 days on Intel i7 4770K depending on the relative orientation of the applied magnetic field with respect to magnetic anisotropy. The magnetization curves for every production run were investigated by applying external magnetic fields H_{ext} with fixed orientation running parallel to z -direction (the normal to the triangular base). The range values of H_{ext} were $+1000\text{kA/m}$ (maximum) and -1000kA/m (minimum) introducing an external magnetic field step $\delta H_{ext} = 4\text{kA/m}$ [38].

2.2 Skyrmion number computation

The calculation of skyrmion number S necessitates the knowledge of the computed normalized magnetization vector \mathbf{m} obtained from the solution of LLG equations. Once the finite element approximation of the normalized magnetization \mathbf{m}_h has been computed, the skyrmion number S_h , following (1), is approximated by

$$S_h = \frac{1}{4\pi} \sum_{e=1}^{N_e} \mathbf{m}_h^e \cdot \left(\frac{\partial \mathbf{m}_h^e}{\partial x} \times \frac{\partial \mathbf{m}_h^e}{\partial y} \right) |A_e|. \quad (4)$$

where m_h, S_h are the discrete representations of m, S respectively with e denoting the element and N_e the total number of elements used for the surface domain discretization. It should be noted that throughout the manuscript the symbol S instead of S_h will be used for the computed value of the skyrmion number. The integration takes place over the top or bottom surface boundary of the prism A . Since we are using tetrahedral P1 elements for the discretization of the prism volume, the top (or bottom) surface boundary is comprised of triangles with outwards pointing normal parallel to the $\hat{\mathbf{z}}$ unit vector. Magnetizations are extracted for the top or bottom surface of the magnetic triangular prismatic nanoelement. These particular magneti-

zations located on the surface elements of the two bases are used for the actual computations of S and of the relative topological quantities. It is possible for a magnetic configuration to include more than one skyrmion. Inevitably, the total skyrmion number would be the algebraic sum of its individual skyrmionic configurations. It follows that a structure that locally includes several skyrmions of different polarity or chirality may yield a zero total skyrmion number. The physical significance of this situation may be attributed to the fact that structures with opposing S may be easier to mutually annihilate. Therefore, it is of interest to monitor following [9] the integral of the absolute value of the topological density symbolized with S_{abs} as it describes the existence of topological entities that are masked and washed out when S is calculated through the integral over all surface domain A . The quantity S_{abs} is defined by the relation

$$S_{abs} = \frac{1}{4\pi} \int_A \left| \mathbf{m} \cdot \left(\frac{\partial \mathbf{m}}{\partial x} \times \frac{\partial \mathbf{m}}{\partial y} \right) \right| dA \quad (5)$$

The scalar quantity S_{abs} is injective and provides the necessary distinctness for different skyrmionic states [9]. The stabilization of such magnetic skyrmions is usually linked to the existence of some kind of anisotropic Dzyaloshinskii-Moriya interaction (DMI). Its discrete estimation follows similarly to (4). It is interesting the calculation of skyrmion numbers for micromagnetic configurations in nanoelements since it can reveal information not readily recognizable by simple visual inspection of the micromagnetic configurations. Furthermore, the skyrmion number S as a function of the applied field \mathbf{H}_{ext} along an hysteresis curve can provide quantitative information of the reversal mechanisms and energy barriers involved in the process.

3 Results

3.1 In-plane MCA

In the first system studied the magnetocrystalline anisotropy (MCA) lies within the plane of the triangular nanoelement parallel to x -direction ($\mathbf{K} // [100]$) with the external field \mathbf{H}_{ext} applied along the width of the nanoelement which is parallel to z -direction ($\mathbf{H}_{ext} // [001]$). The \mathbf{H}_{ext} direction is being fixed parallel to z -direction throughout this work for all systems studied. We have calculated the half-hysteresis loop (descending branch of the loop) for the triangular prismatic nanoelements for different MCA values. The $Ku = 100\text{kJ/m}^3$ is presented in **Fig. 2** along with q_{Sk} . Some micromagnetic configurations being formed along the path of the reversal are shown in **Fig. 3**. We present results only for a declining external field H_{ext} since the full hysteresis diagram does not contribute any additional information regarding the magnetization reversal process [38]. Presenting the full hysteresis diagram would inevitably doubled the required computational effort.

Magnetization reversal depicted in **Fig. 2** starts when the normalized magnetization decreases from the saturation value $M/M_s = 1$, and passing through the nucleation field it reaches to $M/M_s = 0$. Then after passing the annihilation field, it attains finally the value $M/M_s = -1$ indicative that all spins have reversed their magnetization vector orientation. During this reversal process the values of S and S_{abs} are computed in order to provide a quantitative description of the skyrmion-like localized configurations in conjunction with the qualitative actual visualization of the normalized magnetization vector \mathbf{m} of the individual spins. Values of S have been calculated for the top and bottom surface of the triangular prismatic nanoelement for various Ku values shown in **Fig. 4** for all magnetic systems in the present investigation. The values of S have the same quantitative and qualitative behavior on top and bottom surface of the nanoelement ensuring the consistency of the numerical calculations. Throughout the manuscript the reported values of skyrmion numbers S, S_{abs} refer to the computed values on the top surface of the nanoelement.

For the MCA value $Ku = 100 \text{ kJ/m}^3$ represented in **Fig. 2** the process of the reversal of spins gives birth to vortex like formations. The value of S emerges from zero and gradually increases; attaining value 0.5, characteristic of magnetic vortex for external magnetic field $H_{ext} = 4.0 \times 10^3 \text{ A/m}$, it reaches the maximum value of $S \approx 0.75$ that can be considered as an incomplete skyrmion for field value close to $H_{ext} = -2.1 \times 10^5 \text{ A/m}$. Note that similar non-integer values of skyrmion number have been reported in confined helimagnetic nanostructures [9] and in thin confined polygonal nanostructures [32]. It is anticipated that in the present finite magnetic system the skyrmion number can be non-integer due to the restricted area of integration A in **Eq. 1** and **Eq. 5** and the essential contribution of magnetostatic energy. The value of $S = 0.5$ describes a vortex like micromagnetic configuration.

Around the external field value of $H_{ext} = 9.2 \times 10^5 \text{ A/m}$ a small step can be detected in the variation of M/M_s reflected also in S and

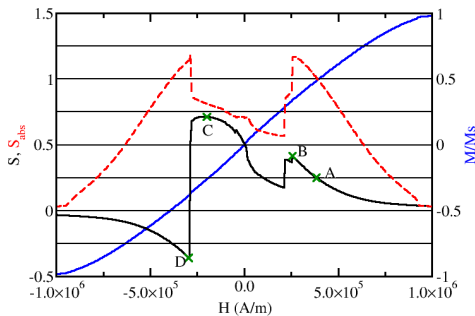


Figure 2: Normalized magnetization (M/M_s) and skyrmion numbers S, S_{abs} during the magnetization reversal process for in plane MCA (along x-direction) with $Ku = 100 \text{ kJ/m}^3$ and $\mathbf{H}_{ext} // [001]$.

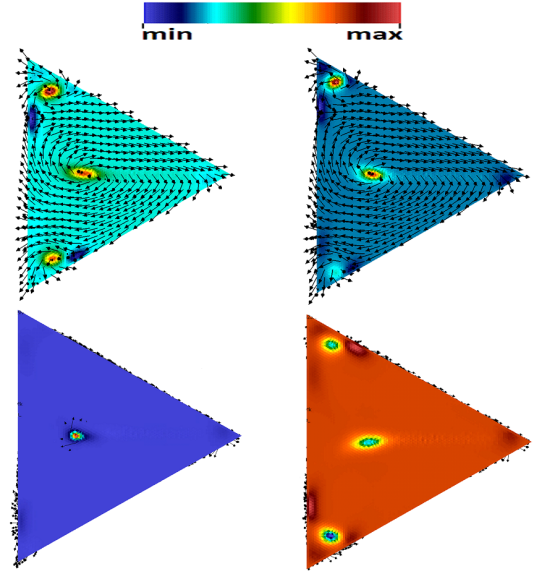


Figure 3: Top view of q_{Sk} at $Ku = 100 \text{ kJ/m}^3$ for MCA being parallel to x-direction and $\mathbf{H}_{ext} // [001]$. From left to right and from top to bottom different values of $H_{ext} = 384, 256, -200, -296 (\times 10^3 \text{ A/m})$ are represented referring to points of A, B, C, D of **Fig. 2**. Local magnetization vectors are shown with arrows superimposed with q_{Sk} . The actual value ranges of q_{Sk}/nm^{-2} are represented in color bars with maximum and minimum values respectively: left top (A $max : 0.00394 - min : -0.00174$), right top (B $max : 0.00693 - min : -0.00203$), left down (C $max : 0.0272 - min : -0.00037$), right down (D $max : 0.00185 - min : -0.00057$).

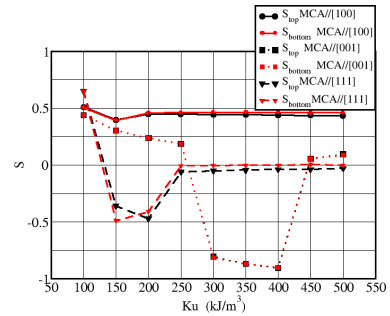


Figure 4: S as a function of K_u for MCA parallel to $[100]$, $[001]$ and $[111]$ directions with $\mathbf{H}_{ext} // [001]$. S is being calculated on the top and bottom surface of the triangular prismatic nanoelement for $H_{ext} = 0 \text{ A/m}$.

magnified in the injective property S_{abs} indicating the origin of magnetization reversal through vortex or skyrmion type mechanisms. In addition, around $H_{ext} = 2.6 \times 10^5 \text{ A/m}$ a jump discontinuity is evident both for S, S_{abs} not captured by the magnetization curve M/M_s . A second jump discontinuity on S is evident around $H_{ext} = -2.7 \times 10^5 \text{ A/m}$ causing the change of S value approximately from 0.7 to -0.4 (relative variation 157%). The aforementioned variation is followed by a change of the sign of S characteristic for a change in the polarity of the vortex type micromagnetic configuration. Further decrease

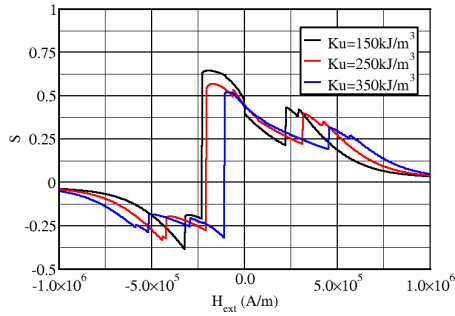


Figure 5: S as a function of H_{ext} for $K_u = 150 - 350 \text{ kJ/m}^3$ with MCA parallel to x-direction and $\mathbf{H}_{ext} // [001]$.

of the external magnetic field causes the continuous decay of S and its annihilation following the final stage of the reversal process. The magnification of jump discontinuities in S_{abs} is anticipated since it is injective and provides the necessary distinctness for different skyrmionic and consequently energy states. Therefore, it is being used in order to detect and explore possible energy barriers during the reversal process. Additionally, in **Fig. 2** differentiation of shapes describing S, S_{abs} reveals that there are local topological density q_{Sk} regions-domains which sum up to zero and therefore mutually annihilate.

Visualizations of micromagnetic configurations are shown in **Fig. 3** for the representative selected external field values depicted in **Fig. 2** and designated as A, B, C, D. The actual topological density q_{Sk} defined in **Eq. 2** represents the "local" skyrmion number of the surface element and is also visualized in **Fig. 3**. This enriched representation gives both qualitative and quantitative description of the actual magnetization configuration. The existence of domains with augmented local topological density is observed close to upper and lower corners of the nanoelement along y -direction for A, B and D points. In addition, an elliptical domain can be observed along the x -axis which is also the direction of the in plane MCA $K_u = 100 \text{ kJ/m}^3$, at the center of the triangular base present in all characteristic points A, B, C, D. These three magnetic entities can be considered as incomplete skyrmions and are present for a wide range of external field values. In **Fig. 3** (point A) the aforementioned magnetic entities expose different magnetization circulations. Those in the corners have a counter clockwise circulation while the domain with augmented q_{Sk} at the center of the triangle has a clockwise circulation.

In **Fig. 5**, skyrmion number S as a function of the external field H_{ext} for different values of K_u is shown. As the magnitude of MCA increases gradually starting from $K_u = 100 \text{ kJ/m}^3$ a similar behavior with **Fig. 2** is observed regarding the qualitative and quantitative characteristics of S . In the cases of $K_u = 150, 250, 350 \text{ kJ/m}^3$ the skyrmion number attains lower values as K_u increases exhibiting jump discontinuities. The calculated maximum (or negative minimum) values denoted as S_{max} for the aforemen-

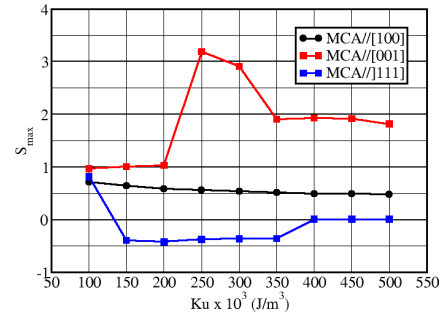


Figure 6: S_{max} as a function K_u for MCA being in plane ($//x$), perpendicular ($//z$) and parallel to $[111]$ direction with respect to the surface base of the nanoelement with the external field $\mathbf{H}_{ext} // [001]$.

tioned cases do not exceed the value $S_{max} = 0.7$ for $K_u = 100 \text{ kJ/m}^3$ represented in **Fig. 5**. For $K_u = 200$ and 300 kJ/m^3 S attains maximum values $0.55 - 0.50$ respectively but at different external magnetic field values H_{ext} . It is evident that the magnetization reversal mechanism necessitates the formation of incomplete skyrmions ($0.5 < S < 1$), vortex-like states ($S = 0.5$) not only for low $K_u = 100$ and 150 kJ/m^3 values but also for the considered as intermediate values of $K_u = 250, 350 \text{ kJ/m}^3$ (**Fig. 6**). Further increase of MCA's values to $K_u = 400, 450, 500 \text{ kJ/m}^3$ expose similar reversal characteristics with S_{max} establishing a plateau region at 0.5 shown in **Fig. 6** characteristic for vortex like reversal process.

The discontinuities detected in case of $K_u = 100 \text{ kJ/m}^3$ are present not only for different values of K_u but for different orientation of the MCA with respect to the surface of the nanoelement e.g. parallel to z -direction. They need further clarification and can be associated to the rich energetic environment having contributions from demagnetization E_{demag} , exchange $E_{exchange}$ and anisotropic E_{anis} energies which can be computed for the systems studied in the present work. Complicated and rich energetic landscapes on the surface of the nanoelement are anticipated. The skyrmion formation is related to the interplay of these energetic contributions.

In order to measure the effect of each individual energy type on the micromagnetic configuration during the magnetization reversal process the absolute relative energy difference $\Delta E_{type}^{rel} = \left| \frac{E_{type}^{i+1} - E_{type}^i}{E_{type}^i} \right| \times 100(\%)$ (where $type$ stands for $anis, exch, demag$) is computed between the consecutive external magnetic field values H_{ext}^i, H_{ext}^{i+1} . As mentioned in **Section 2** the external magnetic field step between consecutive field values is $\delta H_{ext} = 4 \text{ kA/m}$. The values of the relative differences of anisotropy, demagnetization and exchange energies are shown in **Fig. 7** as functions of H_{ext} for MCA values of $K_u = 100, 150 \text{ kJ/m}^3$ superimposed with S_{abs} . It is clear that even in the first steps of the magnetization reversal around values $8.5 - 9.5 \times 10^5 \text{ A/m}$ of the external field for $K_u = 100 \text{ kJ/m}^3$ small steps of the skyrmion number are induced by jump discontinuities on the relative energies and vice versa. These jump

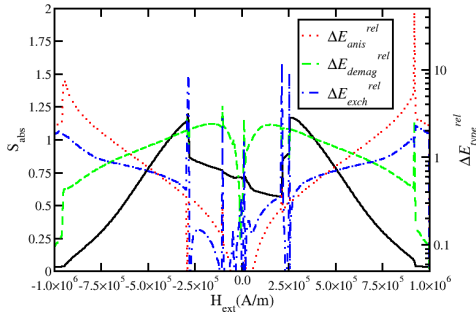


Figure 7: Relative values in % percentages for energetic types of demagnetization, exchange and anisotropic for $K_u = 100$ for MCA parallel to $[100]$.

discontinuities represent the actual energy barriers are pronounced for all types of energies at the beginning of the reversal process with E_{anis} being the more prominent compared to E_{demag} , E_{exch} . The magnetic system and its associated energy should overcome a significant energy barrier in order to start the reversal process in the confined triangular prismatic nanomagnet. In particular, ΔE_{anis}^{rel} attains values close to 42%. Further reduction of the external magnetic field shows continuous behavior up to the value of $H_{ext} = 2.5 \times 10^5$ A/m for S_{abs} . The decrease of the external field H_{ext} drives the continuous and gradual formation of an incomplete skyrmion ($S < 1$). This continuous behaviour is dictated from the continuous behaviour of the total magnetization energy and its energetic components E_{anis} , E_{demag} , E_{exch} . A new energy barrier is observed for S_{abs} around $H_{ext} < 2.5 \times 10^5$ A/m for the exchange energy E_{exch} not followed by the other calculated energies. The value ΔE_{exch}^{rel} of this discontinuity is close to 10%. It is clear that this sharp change at E_{exch} induces the incomplete skyrmion discontinuity not only for $H_{ext} < 2.5 \times 10^5$ A/m but also for the symmetric with respect $H_{ext} = 0$ A/m second maximum around $H_{ext} = -2.5 \times 10^5$ A/m.

In particular, for external fields in the vicinity of $H_{ext} = 0$ A/m a steep descent is evident for ΔE_{demag} . Energy component ΔE_{anis} shows a smoother behavior between the first and last discontinuities having a declining behavior in the first half of the magnetization reversal process where the external field approaches zero value. A continuous increase of the relative change ΔE_{anis} is profound in the second half and final stage of the reversal process. Relative energy difference ΔE_{exch} exhibits an interesting non-continuous behavior having a significant number of sharp discontinuities in the range of $H_{ext} = (-2.5 \text{ to } +2.5) \times 10^5$ A/m external field values. Calculation of energies and relative energies differences for varied K_u showed similar qualitative and quantitative characteristics with the case of $K_u = 100$ kJ/m³. Vortex like or incomplete skyrmion states are triggered by abrupt energy changes and energy barrier crossings.

Further calculations have performed by changing the direction of MCA from x to y direction. This directional change of MCA gives similar physical results re-

garding the formation of vortices despite the fact that MCA's direction remains in plane. This situation with MCA along y -direction differs from MCA lying along x -direction only with respect to the subtle effects of the edge curling on the nucleation process.

3.2 Perpendicular MCA

It is challenging to investigate the effects associated with MCA when is set to z -direction which is the direction normal to the basis surface of the triangular FePt nanoelement. As the vortex-like formations in this system arise from the competition of exchange and magnetostatic energies it is expected that these phenomena will be more pronounced when there is a perpendicular MCA which leads to strong demagnetizing fields. The numerical calculations showed that the dependence of S for the lowest MCA value $K_u = 100$ kJ/m³ is quite similar to the case of in-plane MCA directions exhibiting the same magnetization reversal process. The magnetic system case with $K_u = 150$ kJ/m³ is presented in **Fig. 8**. Since the K_u value is not high enough to give perpendicular anisotropy as the H_{ext} is reduced the system departs from saturation through a series of topologically non-trivial formations giving a gradual increase of the skyrmion number which attains the maximum value $S \simeq 0.9$ in a plateau region between $H_{ext} = -2.5 \times 10^5$ A/m and $H_{ext} = -5 \times 10^5$ A/m is evident. The aforementioned gradual increase of the skyrmion number S for MCA parallel to z -direction for all K_u values studied starts at lower external field values compared to systems having in plane MCA direction. This external field values retardation can be attributed to the higher energy barrier needed to overcome in order to start the reversal process through skyrmion formation. The critical field signaling skyrmion formation for the different $K_u = 150, 250, 350$ kJ/m³ values for MCA parallel to z -direction is located around $H_{ext} = 3.5 \times 10^5$ A/m (**Fig. 8**) and is considerably lower compared to the external field value of $H_{ext} = 7.5 \times 10^5$ A/m for in-plane MCA (**Fig. 2**).

The behavior is strikingly different when MCA attains the values of $K_u = 250, 350$ kJ/m³ depicted also in **Fig. 8**. For the case where $K_u = 350$ kJ/m³ skyrmionic configurations having negative values emerge for external field values lower than 5.0×10^5 A/m. The micromagnetic configuration in **Fig. 8** hosts one skyrmion located at the center of the nanoparticle. A counter-clockwise circulation (positive circulation) can be identified on the top view of the nanoparticle. The central spins of the skyrmion point inwards (negative polarity) as clearly presented at the bottom view of the spin configuration. Consequently, chirality which is the product of circulation and polarity is negative dictating in this manner the negativity of the skyrmion number.

For the particular case of $K_u = 250$ kJ/m³ regions hosting skyrmions are evident having skyrmion number values close to $S = 3$ in a range of applied external fields from $H_{ext} = -0.3 \times 10^5$ A/m to -5.3×10^5 A/m. In **Fig. 9** micromagnetic configurations with topolog-

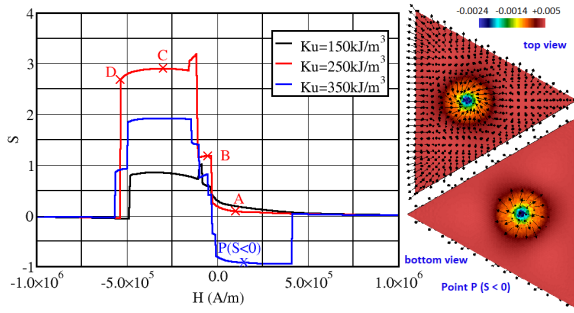


Figure 8: S as a function of H_{ext} for $K_u = 150, 250, 350 \text{ kJ/m}^3$ with MCA running parallel to z -direction alongside with the micromagnetic configuration in top and bottom view (rotated with respect to top view by 60 degrees) for $K_u = 350 \text{ kJ/m}^3$ when skyrmion number attains negative values ($S = -1$) at representative point P.

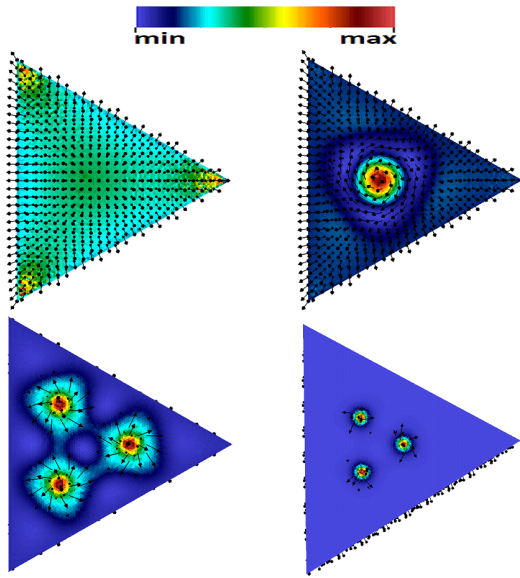


Figure 9: Top view of micromagnetic configuration showing topological density q_{sk} superimposed with the local magnetization for $K_u = 250 \text{ kJ/m}^3$. Different diagrams depict the four points A, B, C, D of Fig. 8 (from left to right and from top to bottom) describing the reversal process. The actual value ranges of q_{sk}/nm^{-2} are represented in color bars with maximum and minimum values respectively: left top (A max : 3.419×10^{-5} – min : -1.117×10^{-6}), right top (B max : 0.00063 – min : -0.00012), left down (C max : 0.00346 – min : -0.00020), right down (D max : 0.00063 – min : -0.00012).

ical density q_{sk} superimposed with the local magnetization vector are presented. Different diagrams depict four representative points A, B, C, D in four characteristic regions during the reversal process of the S variation with the external field H_{ext} . In Fig. 9 (point A in Fig. 8 for $K_u = 250 \text{ kJ/m}^3$) skyrmion is under development. Regions of augmented q_{sk} are evident exactly at the triangle's corners. Lower values of q_{sk} can be seen at the center of the triangular base of the nanoelement. Point B is located at a skyrmion num-

ber S discontinuity with actual value close to $S = 1$. The respective isosurfaces of q_{sk} for point B reveal the existence of one skyrmion located at the center of the triangular prismatic nanoelement.

Points C, D represent micromagnetic configurations hosting three skyrmions. The centers of the skyrmions define an equilateral triangle in both micromagnetic configurations. The essential difference of the skyrmions present in C and D points is their actual size. Skyrmions of point C are larger compared to the respective three skyrmions in D although they have the same circular shapes and location. This can be attributed to the fact that while the sizes in skyrmions of C (Fig. 9 (C)) are larger than those of D (Fig. 9 (D)) the topological densities q_{sk} are higher in D in order to compensate the lower skyrmion surface contributing to the total triangular surface base integration giving in both cases C and D a total skyrmion number equal to 3. Representative values of the maximum q_{sk} on the surface element are $q_{sk,C} = 0.003462 < q_{sk,D} = 0.02181$.

In Fig. 6 the maximum values of S denoted as S_{max} are reported for MCA parallel to z -direction. Moreover, representative configurations depicted for external field values corresponding to S_{max} showing q_{sk} superimposed with magnetization are presented in Fig. 10. For the case where $K_u = 200 \text{ kJ/m}^3$ at the center of the triangular base a clear and complete skyrmion emerges. It has an almost perfect circular shape with the higher values of q_{sk} located at the center mitigating when moving away but along the circle's radius. The magnetization vectors have a counter-clockwise circulation around the skyrmion. In case where $K_u = 250 \text{ kJ/m}^3$ and $S_{max} \approx 3.25$ extended regions located at the triangle's vertices running along the edges of the triangular base are evident. This magnetic configuration significantly differs from the configuration having three well developed skyrmions defining segregated and distinct regions presented in Fig. 9 (point C). These multiple skyrmions or clusters of skyrmions on the surface of the triangular disk are evident and the actual calculation of S gives values during the reversal process in the range of $1 \leq S < 4$ for all MCA values studied having perpendicular anisotropy. The maximum value $S_{max} = 3$ for the case of $K_u = 300 \text{ kJ/m}^3$ is also depicted in Fig. 10 exposing three skyrmions located in extended circular regions.

The increase of the MCA value from $K_u = 150 \text{ kJ/m}^3$ to 500 kJ/m^3 plays a dramatic effect in the magnetization reversal process and the creation of skyrmion regions. Particularly, in the cases where K_u attains values beyond 300 kJ/m^3 reaching 500 kJ/m^3 the maximum of skyrmion number S establishes a plateau at $S = 2$ indicative of the formation of two skyrmions on the surface of the nanoelement. The case of $K_u = 350 \text{ kJ/m}^3$ where $S_{max} = 2$ is representative and is shown in Fig. 10. The two skyrmions are exactly located along the height of the triangle (parallel to x -direction) having different shapes resembling different perturbations of the circular shape. The formation and actual detection of skyrmions can be revealed by visu-

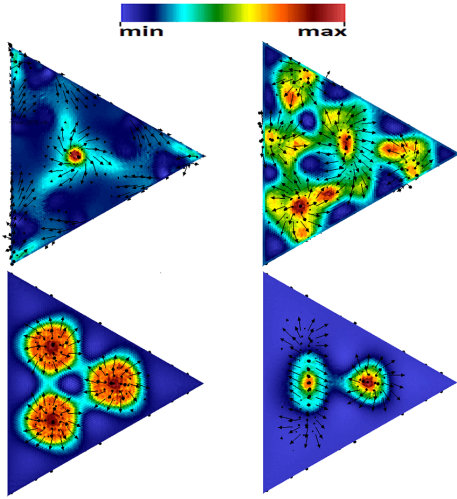


Figure 10: Top view of micromagnetic configurations referring to S_{max} for $Ku=200, 250, 300, 350 \text{ kJ/m}^3$ (from left to right and from top to bottom) for MCA being parallel to z-direction. Magnetization shown with arrows superimposed with q_{Sk} . The actual value ranges of q_{Sk}/nm^{-2} are represented in color bars with maximum and minimum values respectively: left top ($Ku=200 \text{ kJ/m}^3$, $max : 0.00342 - min : -0.00643$), right top ($Ku=250 \text{ kJ/m}^3$, $max : 0.00175 - min : -0.00043$), left down ($Ku=300 \text{ kJ/m}^3$, $max : 0.00135 - min : -0.00020$), right down ($Ku=350 \text{ kJ/m}^3$, $max : 0.00322 - min : -9.61 \times 10^{-5}$).

alizing the actual reversal process. A quantitative and coherent picture can be provided by the calculation of S .

Computations of relative energy differences accompanied by S_{abs} are depicted in **Fig. 11** for $Ku=250 \text{ kJ/m}^3$ which is the case showed the formation of three skyrmions. As it is already commented the first steps of the magnetization reversal for MCA normal to nanoelement's surface start at external field values H_{ext} significantly lower ($< 5 \times 10^5 \text{ A/m}$) compared to the case of in-plane MCA. Following S_{abs} and relative energies variation with respect to external field, energy barriers are present around $H_{ext}=5 \times 10^5 \text{ A/m}$ for all the components of energy. Particularly in **Fig. 11** for $Ku=250 \text{ kJ/m}^3$, ΔE_{exch}^{rel} is close 90% and is the most prominent jump discontinuity compared to ΔE_{anis}^{rel} , ΔE_{demag}^{rel} whose jumps are around 10%. It should also noted that E_{anis}^{rel} exhibits a 90% jump, which is twice as much as the one observed in the case of in plane anisotropy at $Ku=100 \text{ kJ/m}^3$ which was calculated to 42%. The reduction of the external magnetic field affects in a continuous manner the different magnetic energies up to the value of $H_{ext}=0 \text{ A/m}$. In the vicinity of the zero for negative external fields new jump discontinuities are evident for all energies. The decrease of external field H_{ext} drives the continuous and gradual formation followed by energetic and therefore skyrmionic discontinuity events. Complete and incomplete skyrmions are present having values

$1 < S < 4$. Rich energy patterns and textures are clear having similar behaviour not only for $Ku=250 \text{ kJ/m}^3$ but for all Ku values studied when MCA is normal to the nanoelements' base.

Fig. 12 represents the relative energies for characteristic points selected from **Fig. 11** at $Ku=250 \text{ kJ/m}^3$. Energies $E_{anis}, E_{exch}, E_{demag}$ are grouped and shown in five different points. The grouped energies $\{A_i, D_i, E_i\}$ associated with point i ($i=1, \dots, 5$) are depicted at the same or approximately the same $H_{ext,i}$ value. At point $A1$ before crossing the energy barrier, E_{anis} develops an inner triangular region with values lower compared to the maximum values located at the sides of the nanoelement's base. At A_2 point where the barrier is being crossed and skyrmion has been formed the energy distribution follows the skyrmion's location with increasing values of E_{anis} radially moving from the center towards the outer circular domain of skyrmion. Energy isosurfaces for point $A3$ expose three new developed regions in the vicinity of the nanoelement's base vertices. Point $A4$ represents a local energy minimum of E_{anis} in which around the skyrmion domain at the center well developed stripe-like energy domains running parallel to nanoelement's edges are evident. Point $A5$ is the location where the highest energy barrier is detected. From the contour plot is evident that the energy follows exactly the location of the multiple skyrmions formed. Calculation of E_{demag} provides the same qualitative behavior with the subtle difference on point $D1$ at almost identical H_{ext} value with $A1$ where E_{demag} has a uniform distribution on the nanoelement's base. The calculated exchange energy E_{exch} distribution follows the formation process of skyrmions. At point $E1$ high energy regions are located at the vertices of the nanoelement in contrast to E_{anis} . The competition between these energies and energy barrier crossings gives birth to skyrmion magnetic configurations.

3.3 MCA parallel to [111]

In addition to MCA lying on the surface or being normal to the surface of the nanoelement the magneto-crystalline anisotropy is set parallel to [111] direction. The latter case is of interest as in many instances

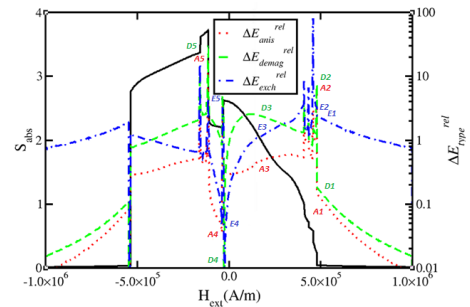


Figure 11: Values in % percentages for relative energy differences of demagnetization, exchange and anisotropic for $Ku=250 \text{ kJ/m}^3$ for MCA parallel to [001].

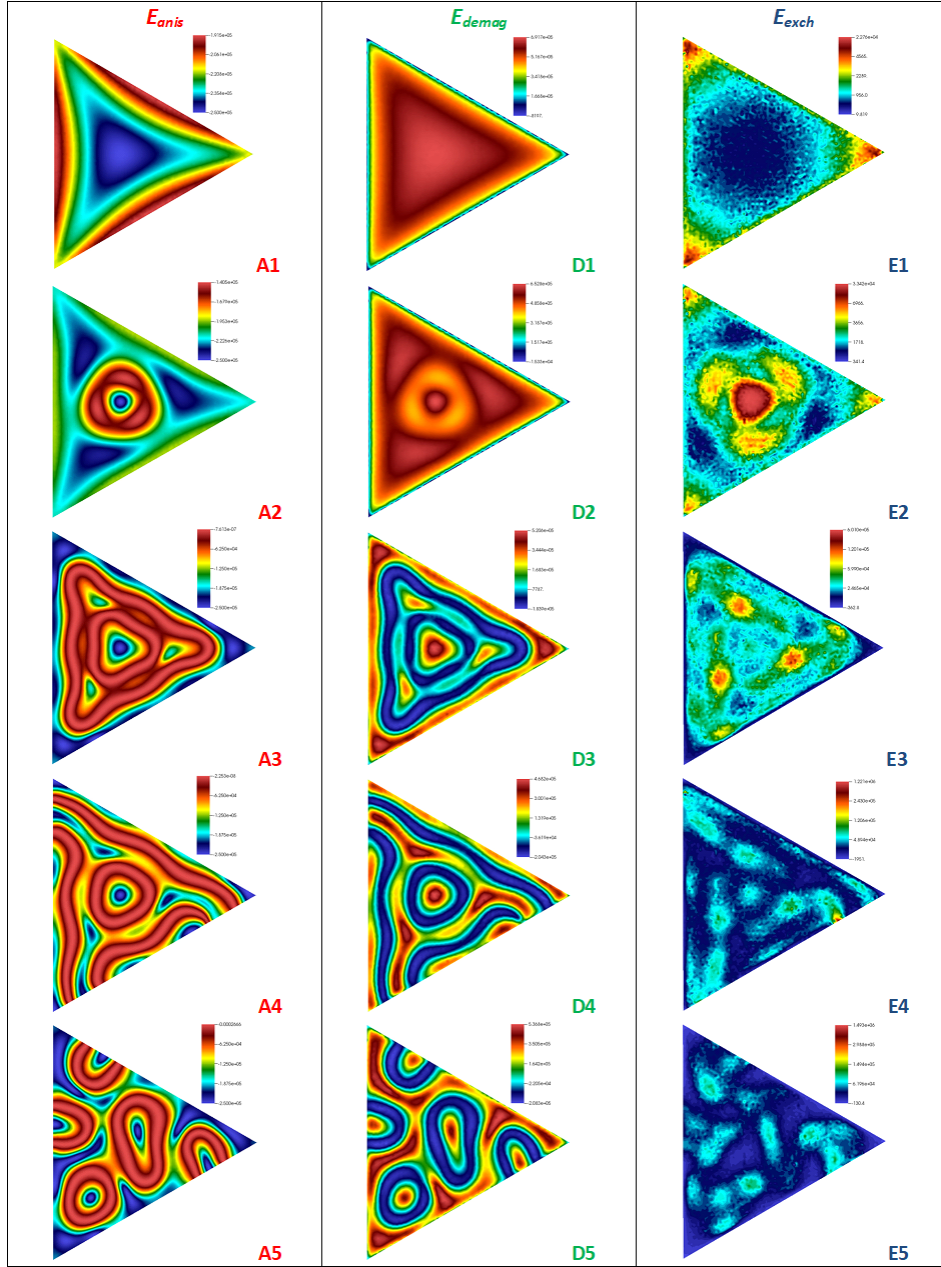


Figure 12: Demagnetization, exchange, and anisotropic energies for $Ku=250\text{kJ/m}^3$ for selected points during the reversal process chosen from **Fig. 11**.

FePt and CoPt films tend to grow with their [111] crystallographic directions resulting an angle of 54.7° to the film normal [1]. The numerical simulation results are presented for S in **Fig. 4** as a function of Ku fixing external field value at $H_{ext}=0\text{A/m}$. At $Ku=100\text{kJ/m}^3$ skyrmion number is close to value $S=0.7$. By increasing MCA up to $Ku=250\text{kJ/m}^3$ skyrmion number reduces attaining negative but non-zero values for external field $H_{ext}=0\text{A/m}$. This is an interesting fact and significantly differentiates compared to the cases where MCA is parallel to x and z (in the majority of Ku values studied) directions where positive skyrmion numbers are obtained. The negative values originate from the negative chirality (circulation \times polarity) of the high skyrmion density q_{Sk} region that can be seen in **Fig. 13**.

The maximum skyrmion number value S_{max} as a function of external field for different MCA values is represented in **Fig. 6**. Topological quantity S_{max} attains negative values in contrast to the cases where MCA is in-plane or perpendicular to the nanoelement's base. For $S_{max} < 0$ the respective MCA value range is $Ku=150-350\text{kJ/m}^3$. Calculation of the skyrmion number at different external field values for the representative $Ku=150, 250, 350\text{kJ/m}^3$ values are shown in **Fig. 13**. Evident is the manifestation of micromagnetic configurations mainly having negative skyrmion numbers for external fields ranging from $H_{ext}=5 \times 10^5\text{A/m}$ to approximately $H_{ext}=-2 \times 10^5\text{A/m}$. The minimum value of S is observed for the case of $Ku=150\text{kJ/m}^3$ and is close to $S=-0.4$. For the three different Ku values shown

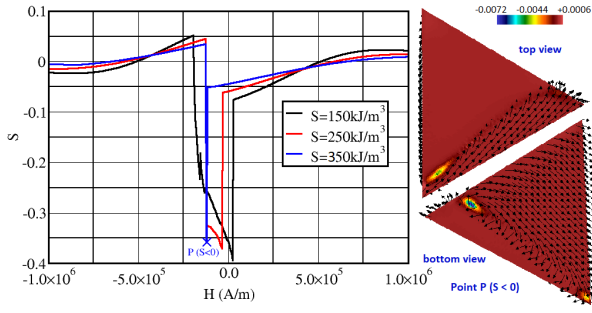


Figure 13: S as a function of H_{ext} for $Ku = 150, 250, 350 \text{ kJ/m}^3$ with MCA running parallel to $[111]$ direction alongside with the micromagnetic configuration in top and bottom view (rotated with respect to top view by 60 degrees) for representative point P with $S < 0$ at $Ku = 350 \text{ kJ/m}^3$.

in **Fig. 13** the crossover to negative S happens at $H_{ext} = 5 \times 10^5 \text{ A/m}$. Also the maximum antivortex states are located at the vicinity of zero external magnetic field which significantly differentiate compared to the previous studied cases.

Conclusions

The topological invariant known as skyrmion number S has been calculated for FePt triangular prism nanoelements with different directions and magnitude of MCA for varying magnitude of the external magnetic field H_{ext} . The direction of the external field \mathbf{H}_{ext} was normal to nanoelement's surface in all conducted numerical simulations. Magnetization configurations during reversal process were studied. It was possible to explore the formation of skyrmionic regions and qualitatively-quantitatively characterize them by a variety of calculated properties such as the skyrmion number, the different contributions on the magnetic energy such as demagnetization energy, exchange energy and uniaxial anisotropy energy and visualization of the micromagnetic configurations. Skyrmionic magnetic configurations have been detected in high symmetry positions with respect to the geometry of the triangular prism having skyrmion number greater than one ($S > 1$) for the case where MCA was normal to nanoelement's base. For MCA attaining values between $Ku = 200 - 500 \text{ kJ/m}^3$ three distinct skyrmions are formed and persist for a range of external fields.

In conjunction with previous studies it is clear that magnetic skyrmions can be produced in a wide range of external fields just by tuning MCA's magnitude and direction, even in the absence of chiral interactions such as Dzyaloshinsky-Moriya. It is challenging to extent the numerical simulations including thermal effects in the form of Brownian term in LLG equation in order to investigate the formation of skyrmions at room temperature.

Acknowledgments

V.D. Stavrou would like to thank the State Scholarship Foundation of Greece (IKY) for the financial support under the scholarship grant (appl. no.14386). We would like to thank Mr. Costas Dimakopoulos for his technical support. Computations have been performed at the Laboratory of Mathematical Modeling and Scientific Computing of the Materials Science Department of the University of Ioannina.

References

- [1] V. Alexandrakis, D. Niarchos, M. Wolff, and I. Panagiotopoulos. Magnetization reversal in CoPt (111) hard/soft bilayers. *Journal of Applied Physics*, 105:063908, 2009.
- [2] Marijan Beg, Maximilian Albert, Marc-Antonio Bisotti, David Cortés-Ortuño, Weiwei Wang, Rebecca Carey, Mark Vousden, Ondrej Hovorka, Chiara Ciccarelli, Charles S. Spencer, Christopher H. Marrows, and Hans Fangohr. Dynamics of skyrmionic states in confined helimagnetic nanostructures. *Phys. Rev. B*, 95:014433, Jan 2017.
- [3] A. Bogdanov. Thermodynamically stable magnetic vortex states in magnetic crystals. *Journal of Magnetism and Magnetic Materials*, 138(3):255–269, 1994.
- [4] A. Bogdanov and A. Hubert. Thermodynamically stable magnetic vortex states in magnetic crystals. *JETP Lett.*, 62:247–251, 1995.
- [5] Felix Büttner, Ivan Lemesh, and Geoffrey S. D. Beach. Theory of isolated magnetic skyrmions: From fundamentals to room temperature applications. *Scientific Reports*, 8:4464, 2018.
- [6] Y. Y. Dai, H. Wang, P. Tao, T. Yang, W. J. Ren, and Z. D. Zhang. Skyrmion ground state and gyration of skyrmions in magnetic nanodisks without the dzyaloshinsky-moriya interaction. *Phys. Rev. B*, 88:054403, Aug 2013.
- [7] Albert Fert, Nicolas Reyren, and Vincent Cros. Magnetic skyrmions: advances in physics and potential applications. *Nature Reviews: Materials*, 2:17031, 2017.
- [8] T. Fischbacher, M. Franchin, G. Bordignon, and H. Fangohr. A systematic approach to multi-physics extensions of finite-element-based micromagnetic simulations: Nmag. *IEEE Trans. Magn.*, 43:2896–2898, 2007.
- [9] T. Fischbacher, M. Franchin, G. Bordignon, and H. Fangohr. Ground state search, hysteretic behaviour, and reversal mechanism of skyrmionic textures in confined helimagnetic nanostructures. *Scientific Reports*, 5:6784, 2015.

- [10] Konstantin Y. Guslienko. Skyrmion State Stability in Magnetic Nanodots with Perpendicular Anisotropy. *IEEE MAGNETICS LETTERS*, 6:4000104, 2015.
- [11] Christian Hanneken, Fabian Otte, André Kubetzka, Bertrand Dupé, Niklas Romming, Kirsten von Bergmann, Roland Wiesendanger, and Stefan Heinze. Electrical detection of magnetic skyrmions by tunnelling non-collinear magnetoresistance. *Nature Nanotechnology*, 10:1039–1042, 2015.
- [12] Zhezhi He, Shaahin Angizi, and Deliang Fan. Current-induced dynamics of multiple skyrmions with domain-wall pair and skyrmion-based majority gate design. *IEEE MAGNETICS LETTERS*, 8:4305705, 2017.
- [13] Stefan Heinze, Kirsten von Bergmann, Matthias Menzel, Jens Brede, Andre Kubetzka, Roland Wiesendanger, Gustav Bihlmayer, and Stefan Blugel. Spontaneous atomic-scale magnetic skyrmion lattice in two dimensions. *Nature Physics*, 7:713–718, 2011.
- [14] Junichi Iwasaki, Aron J. Beekman, and Naoto Nagaosa. Theory of magnon-skyrmion scattering in chiral magnets. *Phys. Rev. B*, 89:064412, Feb 2014.
- [15] M. Jaafar, R. Yanes, D. Perez de Lara, O. Chubykalo-Fesenko, A. Asenjo, E. M. Gonzalez, J. V. Anguita, M. Vazquez, and J. L. Vicent. Control of the chirality and polarity of magnetic vortices in triangular nanodots. *Phys. Rev. B*, 81:054439, Feb 2010.
- [16] S. Jeong, M.E. McHenry, and D.E. Laughlin. Growth and characterization of L10 FePt and CoPt $\langle 001 \rangle$ textured polycrystalline thin films. *IEEE Transactions on Magnetics*, 37:1309–1311, 2001.
- [17] Wanjun Jiang, Pramey Upadhyaya, Wei Zhang, Guoqiang Yu, M. Benjamin Jungfleisch, Frank Y. Fradin, John E. Pearson, Yaroslav Tserkovnyak, Kang L. Wang, Olle Heinonen, Suzanne G. E. te Velthuis, and Axel Hoffmann. Blowing magnetic skyrmion bubbles. *Science*, 349(6245):283–286, 2015.
- [18] C. Jin, C. Song, J. Wang, H. Xia, and J. Wang. Topological trajectories of a magnetic skyrmion with in-plane microwave magnetic field. *Journal of Applied Physics*, 122:223901, 2017.
- [19] K.Everschor-Sitte, M. Sitte, T. Valet, A. Abanov, and J. Sinova. Skyrmion production on demand by homogeneous dc currents. *New Journal of Physics*, page 092001, 2017.
- [20] Dong-Hyun Kim, Elena A. Rozhkova, Ilya V. Ulasov, Samuel D. Bader, Tijana Rajh, Maciej S. Lesniak, and Valentyn Novosad. Biofunctionalized magnetic-vortex microdisks for targeted cancer-cell destruction. *Nature Materials*, 9:165–171, 2010.
- [21] S. Komineas and N. Papanicolaou. Topology and dynamics in ferromagnetic media. *Physica D*, 99:81–107, 1996.
- [22] Wataru Koshibae and Naoto Nagaosa. Theory of antiskyrmions in magnets. *Scientific Reports*, 7:10542, 2016.
- [23] Wataru Koshibae and Naoto Nagaosa. Theory of skyrmions in bilayer systems. *Scientific Reports*, 7:42645, 2017.
- [24] J. Li, A. Tan, K.W. Moon, A. Doran, M.A. Marcus, A.T. Young, E. Arenholz, S. Ma, R.F. Yang, C. Hwang, and Z.Q. Qiu. Tailoring the topology of an artificial magnetic skyrmion. *Nature Communications*, 5(4704):1–14, November 2014.
- [25] A. Markou, K. G. Beltsios, L. N. Gergidis, I. Panagiotopoulos, T. Bakas, K. Ellinas, A. Tserepi, L. Stoleriu, R. Tanasa, and A. Stancu. Magnetization reversal in triangular L1 0-FePt nanoislands. *Journal of Magnetism and Magnetic Materials*, 344:224–229, 2013.
- [26] B. F. Miao, L. Sun, Y. W. Wu, X. D. Tao, X. Xiong, Y. Wen, R. X. Cao, P. Wang, D. Wu, Q. F. Zhan, B. You, J. Du, R.W. Li, and H. F. Ding. Experimental realization of two-dimensional artificial skyrmion crystals at room temperature. *Phys. Rev. B*, 90:174411, 2014.
- [27] C. Moreau-Luchaire, C. Moutafis, N. Reyren, J. Sampaio, C. A. F. Vaz, N. Van Horne, K. Bouzehouane, K. Garcia, C. Deranlot, P. Warinck, P. Wöhlhüter, J.M. George, M. Weigand, J. Raabe, V. Cros, and A. Fert. Additive interfacial chiral interaction in multilayers for stabilization of small individual skyrmions at room temperature. *Nature Nanotechnology*, 11:444–448, 2016.
- [28] Jan Müller. Magnetic skyrmions on a two-lane racetrack. *New Journal of Physics*, 19:025002, 2017.
- [29] Y. Nakatani, M. Hayashi, S. Kanai, S. Fukami, and H. Ohno. Electric field control of skyrmions in magnetic nanodisks. *Applied Physics Letters*, 108:152403, 2016.
- [30] NETGEN.
- [31] S. Okamoto, N. Kikuchi, O. Kitakami, T. Miyazaki, Y. Shimada, and K. Fukamichi. Chemical-order-dependent magnetic anisotropy and exchange stiffness constant of FePt (001) epitaxial films. *Phys. Rev. B*, 66:024413, 2002.

- [32] Ryan A. Pepper, Marijan Beg, David Cortés-Ortuño, iñij Thomas Kluyver, Marc-Antonio Bisotti, Rebecca Carey, iñij Mark Vousden, Maximilian Albert and iñij Weiwei Wang, Ondrej Hovorka, and Hans Fangohr. Skyrmion states in thin confined polygonal nanostructures. *Journal of Applied Physics*, 123:093903, 2018.
- [33] N. Romming, C. Hanneken, M. Menzel, J. E. Bickel, B. Wolter, K. von Bergmann, A. Kubetzka, and R. Wiesendanger. Writing and deleting single magnetic skyrmions. *Science*, 341:636–639, 2013.
- [34] N. Romming, A. Kubetzka, C. Hanneken, K. von Bergmann, and R. Wiesendanger. Field-dependent size and shape of single magnetic skyrmions. *Physical Review Letters*, 114:177203, 2015.
- [35] J. Sampaio, V. Cros, S. Rohart, A. Thiaville, and A. Fert. Nucleation, stability and current-induced motion of isolated magnetic skyrmions in nanostructures. *Nature Nanotechnology*, 8:839–844, 2013.
- [36] M.V. Sapozhnikov. Skyrmion lattice in a magnetic film with spatially modulated material parameters. *Journal of Magnetism and Magnetic Materials*, 396:338–344, 2015.
- [37] D.J. Sellmyer, Y. Xu, M. Yan, Y. Sui, J. Zhou, and R. Skomski. Assembly of high-anisotropy L10 FePt nanocomposite films. *Journal of Magnetism and Magnetic Materials*, 303:302–308, 2006.
- [38] V.D. Stavrou, L. N. Gergidis, A. Markou, A. Charalambopoulos, and I. Panagiotopoulos. Micromagnetics of triangular thin film nanoelements. *Journal of Magnetism and Magnetic Materials*, 401:716–723, 2016.
- [39] Martin Stier, Wolfgang Häusler, Thore Posske, Gregor Gurski, and Michael Thorwart. Skyrmion-anti-skyrmion pair creation by in-plane currents. *Phys. Rev. Lett.*, 118:267203, Jun 2017.
- [40] Dusan Stosic, Jeroen Mulders, Bartel Van Waeyenberge, Teresa B. Ludermir, and Milorad V. Milošević. Paths to collapse for isolated skyrmions in few-monolayer ferromagnetic films. *Phys. Rev. B*, 95:214418, Jun 2017.
- [41] S. Stuart, P. Parkin, Masamitsu Hayashi, and Luc Thomas. Magnetic domain-wall racetrack memory. *Science*, 320(5873):190–194, 2008.
- [42] A. Tan, J. Li, A. Scholl, E. Arenholz, A. T. Young, Q. Li, C. Hwang, and Z. Q. Qiu. Topology of spin meron pairs in coupled Ni/Fe/Co/Cu(001) disks. *Physical Review B*, 94:014433, 2016.
- [43] R. Tomasello, E. Martinez, R. Zivieri, L. Torres, M. Carpentieri, and G. Finocchio. A strategy for the design of skyrmion racetrack memories. *Scientific Reports*, 4(6784):17137, 2014.
- [44] Y. Wang, P. Sharma, and A. Makino. Magnetization reversal in a preferred oriented (111) L10 FePt grown on a soft magnetic metallic glass for tilted magnetic recording. *Journal of Physics Condensed Matter*, 24(7), 2012.
- [45] H. Xia, C. Song, C. Jin, J. Wang, J. Wang, and Q. Liu. Skyrmion motion driven by the gradient of voltage-controlled magnetic anisotropy. *Journal of Magnetism and Magnetic Materials*, 458:57–61, 2018.
- [46] Haiyan Xia, Chendong Jin, Chengkun Song, Jinshuai Wang, Jianbo Wang, and Qingfang Liu. Control and manipulation of antiferromagnetic skyrmions in racetrack. *J. Phys. D: Appl. Phys.*, 50:505005, 2017.
- [47] J.W. Yoo, S.J. Lee, J.H. Moon, and K.J. Lee. Phase diagram of a single skyrmion in magnetic nanowires. *IEEE Transactions on Magnetics*, 50:1500504, 2014.
- [48] Xiuzhen Yu, Maxim Mostovoy, Yusuke Tokunaga, Weizhu Zhang, Koji Matsui, Yoshio Kaneko, Naoto Nagaosa, and Magnetic stripes and skyrmions with helicity reversals. *PNAS*, 109(23):8856–8860, 2012.
- [49] S. Zhang, A. K. Petford-Long, and C. Phatak. Creation of artificial skyrmions and antiskyrmions by anisotropy engineering. *Scientific Reports*, 6:131248, 2016.
- [50] X. Zhang, M. Ezawa, and Y. Zhou. Magnetic skyrmion logic gates: conversion, duplication and merging of skyrmions. *Scientific Reports*, 5:1500504, 2015.
- [51] Y. Zhou, E. Iacocca, A.A. Awad, R.K. Dumas, F.C. Zhang, H.B. Braun, and J. Akerman. Dynamically stabilized magnetic skyrmions. *Nature Communications*, 6:8193, 2015.